




Influence of effective nucleon mass on equation of state for supernova simulations and neutron stars

SHUYING LI,¹ JUNBO PANG,¹ HONG SHEN ¹, JINNIU HU ¹ AND KOHSUKE SUMIYOSHI ²

¹*School of Physics, Nankai University, Tianjin 300071, People's Republic of China*

²*National Institute of Technology, Numazu College, Shizuoka 410-8501, Japan*

ABSTRACT

We investigate the influence of the effective nucleon mass on the equation of state (EOS), which is constructed for simulations of core-collapse supernovae and binary neutron star mergers, within the relativistic mean-field (RMF) framework. The study introduces a new RMF parameter set, TM1m, which is a modification of the TM1e model with an adjusted effective mass, maintaining the saturation properties of nuclear matter. The TM1m model, with a larger effective mass ratio ($M^*/M \sim 0.8$) compared to the TM1e model ($M^*/M \sim 0.63$), is employed to construct a new EOS table, EOS5. This EOS table is designed to offer insights into the influence of the effective nucleon mass on the EOS within a relativistic framework, particularly above the saturation density. The results of EOS5 are compared with those obtained from other models, including both relativistic and nonrelativistic approaches. The properties of cold neutron stars, calculated using the TM1m model, are compatible with the existence of a $2 M_\odot$ pulsar and the latest constraints on the tidal deformability and radii of a canonical $1.4 M_\odot$ neutron star, derived from astrophysical observations.

Unified Astronomy Thesaurus concepts: [Core-collapse supernovae \(304\)](#); [Neutron stars \(1108\)](#)

1. INTRODUCTION

The equation of state (EOS) of hot and dense matter is an essential ingredient for understanding astrophysical phenomena, such as core-collapse supernovae, proto-neutron star cooling, and binary neutron star mergers (Oertel et al. 2017). The EOS should cover a wide range of temperatures T , proton fractions Y_p , and baryon mass densities ρ_B , exhibiting a complex phase diagram. At low temperatures and subsaturation densities, the matter is nonuniform, with heavy nuclei forming to lower the free energy of the system. When the density reaches about half of the nuclear saturation density, heavy nuclei tend to dissolve into a homogeneous nuclear liquid. At the density higher than two to three times the nuclear saturation density, non-nucleonic degrees of freedom, such as hyperons and quarks, may occur and soften the EOS of dense matter (Maruyama et al. 2007; Yasutake et al. 2014; Weber et al. 2019; Huang et al. 2022a,b; Sumiyoshi et al. 2023). On the other hand, with increasing temperature T , the density

range of nonuniform matter shrinks and, finally, heavy nuclei cannot be formed above a critical value of ~ 14 MeV (Shen et al. 2011b).

Owing to the complexity of the phase behavior of stellar matter, constructing a full EOS for general usage in astrophysical applications is a daunting task. A set of the available EOSs has been summarized in the review by Oertel et al. (2017), which can also be obtained from the public database CompOSE (Typel et al. 2022). Over the past decades, the two most commonly used EOSs in astrophysical simulations have been the EOS of Lattimer & Swesty (1991) and that of Shen et al. (1998a). The Lattimer-Swesty EOS was based on the compressible liquid drop (CLD) model with a nonrelativistic Skyrme force. In contrast, the Shen EOS employed the relativistic mean-field (RMF) model and the Thomas-Fermi approximation with a parameterized nucleon distribution for the description of nonuniform matter. In these EOSs, the single-nucleus approximation (SNA) was adopted, which meant that only a single representative nucleus was considered instead of an ensemble of nuclei. Recently, EOS tables have been developed beyond the SNA, by including multiple nuclei in nuclear statistical equilibrium (NSE) (Hempel & Schaffner-Bielich 2010; Shen et al. 2011a; Steiner et al. 2013; Fu-

shennankai@gmail.com

hujinniu@nankai.edu.cn

rusawa et al. 2017a; Schneider et al. 2017; Raduta & Gulminelli 2019). It has been shown that considering the nuclear distributions may play an important role in the neutrino-matter interactions (Nagakura et al. 2019), but have less influence on the thermodynamic quantities of dense matter (Hempel & Schaffner-Bielich 2010). Furthermore, microscopic approaches based on realistic nuclear forces have also been used to construct the EOS table for astrophysical simulations (Togashi et al. 2017; Furusawa et al. 2017b, 2020).

The first version of the Shen EOS (EOS1) was published in Shen et al. (1998a), in which we first provided the EOS in three-dimensional (T, Y_p, ρ_B) tabular form, including the thermodynamic and compositional quantities needed in the applications. This EOS design is convenient for performing supernova simulations and has been commonly used in building EOS tables in subsequent years (Typel et al. 2015). In Shen et al. (2011b), we recalculated the EOS table with improved designs of ranges and grids, according to the requirements of the EOS users. The improved EOS tables were referred to as: (a) EOS2, which includes only the nucleonic degree of freedom; and (b) EOS3, which incorporates additional Λ hyperons. Both EOS1 and EOS2 were based on the RMF approach, using the TM1 parameterization for nuclear interactions. The nonuniform matter, consisting of a lattice of heavy nuclei, was described within the Thomas-Fermi approximation, in combination with assumed nucleon distribution functions and a free-energy minimization procedure. The TM1 model provides a satisfactory description for finite nuclei and predicts a maximum neutron star mass of $2.18 M_\odot$ with nucleonic degrees of freedom only. However, the resulting neutron star radii seem to be excessively large (Shen et al. 1998b, 2020). Remarkable progress in astrophysical observations has been achieved over the last decade, providing crucial constraints on the EOS of dense matter. A stringent constraint comes from the precise mass measurements of massive pulsars—PSR J1614-2230 ($1.908 \pm 0.016 M_\odot$; Arzoumanian et al. (2018)), PSR J0348+0432 ($2.01 \pm 0.04 M_\odot$; Antoniadis et al. (2013)), and PSR J0740+6620 ($2.08 \pm 0.07 M_\odot$; Fonseca et al. (2021))—which require the predicted maximum neutron star mass to be larger than $\sim 2 M_\odot$. The first detection of gravitational waves from a binary neutron star merger, GW170817 (Abbott et al. 2017, 2018) provided an upper limit on the tidal deformability and constrained the radius of neutron stars (Fattoyev et al. 2018; Most et al. 2018). Furthermore, the recent observations by the Neutron Star Interior Composition Explorer (NICER) for PSR J0030+0451 (Miller et al. 2019; Riley et al. 2019) and PSR J0740+6620 (Miller et al.

2021; Riley et al. 2021) provided simultaneous measurements of the mass and radius of neutron stars, which offer strong constraints on the EOS of dense matter. Considering the progress in astrophysical observations, we constructed a revised version of the Shen EOS (EOS4), based on an extended TM1 model, referred to as the TM1e model, in Shen et al. (2020). It is noteworthy that the TM1e and original TM1 models have identical properties for symmetric nuclear matter but exhibit different behaviors of the symmetry energy. The TM1e model has a symmetry energy slope of $L = 40$ MeV, significantly smaller than the value of $L = 111$ MeV in the original TM1 model. Consequently, it predicts smaller neutron star radii, which are supported by astrophysical observations (Shen et al. 2020). By comparing the results from astrophysical simulations using EOS4 and EOS2, one can estimate the effects of the symmetry energy and its density dependence (Sumiyoshi et al. 2019).

Recently, it was reported in Schneider et al. (2019) and Yasin et al. (2020) that the effective nucleon mass has a decisive effect on supernova explosions through pressure difference, proto-neutron star contraction, and neutrino emission (see also Andersen et al. (2021) for gravitational waves). A larger effective mass leads to smaller thermal contributions to the pressure, which results in more rapid contraction and aids the shock evolution in faster explosions. However, in their calculations, the influence of the effective mass was investigated using a set of Skyrme-type EOSs, by varying the effective nucleon mass at saturation density, which was treated as a model parameter within a nonrelativistic framework. In Nakazato & Suzuki (2019), the influence of the effective nucleon mass on the cooling process of a proto-neutron star was investigated using a series of phenomenological EOSs, in which the effective nucleon mass, as a model parameter, was set to be constant. It is widely accepted that the effective mass should be density-dependent and can be incorporated more consistently in a relativistic framework than in nonrelativistic approaches.

In the present work, we will adjust the RMF parameters based on the TM1e parameterization, so that the saturation properties obtained by the new parameterization remain the same as those of TM1e, but with different effective masses. The TM1e model predicts an effective mass ratio $M^*/M \sim 0.63$ at the saturation density n_0 , while the new parameterization, referred to hereafter as the TM1m model, sets this ratio to be $M^*/M \sim 0.8$. Note that the effective masses in the TM1e and TM1 models are identical, due to having the same isoscalar properties.

Currently, there is no direct constraint on the effective nucleon mass from experimental observations. In nonrelativistic Skyrme models, the effective mass at saturation density is often treated as a model parameter, which can be tuned to different values within the range of $M^*/M \sim 0.5 - 1.0$, while keeping other saturation properties unchanged (Nakazato & Suzuki 2019; Schneider et al. 2019). In RMF models, the effective mass, defined by $M^* = M + g_\sigma \sigma$, is reduced from the free nucleon mass by a large negative scalar potential, $U_S = g_\sigma \sigma$. The saturation mechanism of symmetric nuclear matter in the RMF models can be achieved by a delicate balance between large negative scalar and positive vector potentials (Serot & Walecka 1986). As a consequence, the effective mass at saturation density obtained in well-known RMF models (Serot & Walecka 1986; Lalazisis et al. 1997; Steiner et al. 2013; Chen & Piekarewicz 2014; Dutra et al. 2014; Miyatsu et al. 2024) generally lies within a narrow range, $M^*/M \sim 0.54 - 0.8$. In Choi et al. (2021), the authors investigated the impacts of the effective nucleon mass on the nuclear and neutron star properties within the range of $0.5 \leq M^*/M \leq 0.8$. It is almost impossible to enforce a very large effective mass in the RMF model, because small scalar and vector potentials, which are related to large effective masses, will not be able to reproduce the empirical saturation point of symmetric nuclear matter. Therefore, we prefer to set $M^*/M \sim 0.8$ in the TM1m model and compare to the TM1e model with $M^*/M \sim 0.63$, while keeping other saturation properties unchanged.

In order to investigate the impact of the effective nucleon mass on astrophysical simulations, we construct a new EOS table (referred to as EOS5) using the TM1m model. We prepare all quantities in the EOS table for uniform matter at densities higher than $\sim 10^{14}$ g/cm³ by using the TM1m model, which can then be combined with the nonuniform part of the Shen EOS4 at low densities to generate the final EOS table, as is often done in the literature Ishizuka et al. (2008); Sumiyoshi et al. (2019). By switching only the uniform matter in EOS5 with the TM1m model, we clarify the influence of effective mass at high densities. The application of EOS5 with $M^*/M \sim 0.8$, compared to EOS4 with $M^*/M \sim 0.63$, can be used to clarify the impact of effective mass on astrophysical simulations, such as core-collapse supernovae, proto-neutron star cooling, and binary neutron star mergers.

This paper is arranged as follows. In Section 2, we briefly describe the RMF approach used for constructing the EOS table and compare different parameter sets. In Section 3, we present numerical results using the new parameterization TM1m and compare them to those ob-

tained from other models, including both relativistic and nonrelativistic approaches. Finally, a summary and conclusions are presented in Section 4.

2. MODEL AND PARAMETERS

In order to make the article self-contained, we give a brief description of the RMF model used for constructing the EOS table. We employ the RMF model, including nonlinear terms for the σ and ω mesons and an additional ω - ρ coupling term. Nucleons interact through the exchange of mesons—specifically, scalar σ , vector ω , and isovector ρ mesons (Bao et al. 2014; Shen et al. 2020). The nucleonic Lagrangian density can be expressed as

$$\begin{aligned} \mathcal{L}_{\text{RMF}} = & \sum_{i=p,n} \bar{\psi}_i [i\gamma_\mu \partial^\mu - (M + g_\sigma \sigma) \\ & - \gamma_\mu \left(g_\omega \omega^\mu + \frac{g_\rho}{2} \tau_a \rho^{a\mu} \right)] \psi_i \\ & + \frac{1}{2} \partial_\mu \sigma \partial^\mu \sigma - \frac{1}{2} m_\sigma^2 \sigma^2 - \frac{1}{3} g_2 \sigma^3 - \frac{1}{4} g_3 \sigma^4 \\ & - \frac{1}{4} W_{\mu\nu} W^{\mu\nu} + \frac{1}{2} m_\omega^2 \omega_\mu \omega^\mu + \frac{1}{4} c_3 (\omega_\mu \omega^\mu)^2 \\ & - \frac{1}{4} R_{\mu\nu}^a R^{a\mu\nu} + \frac{1}{2} m_\rho^2 \rho_\mu^a \rho^{a\mu} \\ & + \Lambda_v (g_\omega^2 \omega_\mu \omega^\mu) (g_\rho^2 \rho_\mu^a \rho^{a\mu}), \end{aligned} \quad (1)$$

where $W^{\mu\nu}$ and $R^{a\mu\nu}$ represent the antisymmetric field tensors corresponding to ω^μ and $\rho^{a\mu}$, respectively. Within the mean-field approximation, the meson field operators are replaced by their expectation values. In a static uniform system, the nonzero components are given by $\sigma = \langle \sigma \rangle$, $\omega = \langle \omega^0 \rangle$, and $\rho = \langle \rho^{30} \rangle$. The equations of motion for nucleons and mesons are derived from the Lagrangian density, and these coupled equations can be solved self-consistently within the RMF framework.

In order to explore the influence of the effective nucleon mass on astrophysical simulations, we refit the RMF parameters based on the TM1e model used in constructing the Shen EOS4 (Shen et al. 2020). A new parameter set, referred to as TM1m, is introduced with a larger effective mass, while all other saturation properties remain identical to those of TM1e. In Table 1, we present the coupling constants of the TM1m, TM1e, and original TM1 models, while the corresponding saturation properties are listed in Table 2. It is shown that the main difference between TM1m and TM1e is the effective mass, i.e., $M^*/M \sim 0.8$ in the TM1m model and $M^*/M \sim 0.63$ in the TM1e model. On the other hand, the difference between TM1e and TM1 lies in the density dependence of the symmetry energy, with the symmetry energy slope being $L = 40$ MeV in the TM1e model and $L = 111$ MeV in the original TM1 model, respectively.

Table 1. Coupling constants of the TM1m, TM1e, and original TM1 models.

Model	g_σ	g_ω	g_ρ	g_2 [fm $^{-1}$]	g_3	c_3	Λ_ν
TM1m	7.93528	8.63169	11.51296	-11.51628	54.88715	0.00025	0.09326
TM1e	10.0289	12.6139	13.9714	-7.2325	0.6183	71.3075	0.0429
TM1	10.0289	12.6139	9.2644	-7.2325	0.6183	71.3075	0.0000

Table 2. Nuclear matter properties obtained in the TM1m, TM1e, and original TM1 models.

Model	n_0 (fm $^{-3}$)	E/A (MeV)	K (MeV)	E_{sym} (MeV)	L (MeV)	M^*/M
TM1m	0.145	-16.3	281	31.4	40	0.793
TM1e	0.145	-16.3	281	31.4	40	0.634
TM1	0.145	-16.3	281	36.9	111	0.634
SFHo	0.158	-16.2	245	31.6	47	0.761
Skyrme-SLy4	0.160	-16.0	230	32.0	46	0.694

Note. The saturation density and the energy per particle are denoted by n_0 and E/A, the incompressibility by K , the symmetry energy and its slope by E_{sym} and L , and the effective mass ratio by M^*/M . The results obtained from the SFHo model (Steiner et al. 2013) and the nonrelativistic Skyrme-SLy4 model (Chabanat et al. 1998) are also listed for comparison.

We prefer to set $M^*/M \sim 0.8$ at saturation density in the TM1m model, which is considered to be a relatively high and achievable value within the RMF approach (Dutra et al. 2014). It is noteworthy that the allowed region for the ratio M^*/M in the RMF model is significantly restricted compared to nonrelativistic Skyrme models. This is because the saturation mechanism of symmetric nuclear matter in the RMF approach is due to a delicate balance between large negative scalar and positive vector potentials. An excessively large effective mass M^* correlates with scalar and vector potentials that are too weak to accurately reproduce the empirical saturation point. In fact, the effective mass at saturation density obtained in several well-known RMF models lies within a narrow range. For example, the linear Walecka model (Serot & Walecka 1986) has $M^*/M = 0.54$, while this ratio is around 0.6 in the nonlinear RMF models with NL3 (Lalazisis et al. 1997), IUFSU (Fattoyev et al. 2010), FSUGold2 (Chen & Piekarewicz 2014), and FSUGarnet (Chen & Piekarewicz 2015) parameterizations. For comparison, we include in Table 2 the results from an RMF model with the SFHo parameterization (Steiner et al. 2013) and a nonrelativistic Skyrme model with the SLy4 parameterization (Chabanat et al. 1998). The SFHo

model has been widely used in astrophysical simulations (Oertel et al. 2017), in which $M^*/M = 0.76$ is obtained and several additional couplings are introduced (Steiner et al. 2013). As a typical Skyrme force, the SLy4 model is frequently utilized for both nuclear structure calculations and astrophysical simulations (Oertel et al. 2017; Schneider et al. 2017), employing a zero-range effective interaction within the non-relativistic framework. We intend to compare the results obtained from the RMF models with those from the Skyrme-SLy4 model to explore possible relativistic effects, particularly at high densities.

In Figure 1, we plot the energy per baryon E/A of symmetric nuclear matter and neutron matter as a function of the baryon number density n_B . It is shown that the behaviors of symmetric nuclear matter are exactly the same between the TM1e and TM1 models, whereas those of the TM1m model become slightly lower as the density increases. This is because the larger effective mass in the TM1m model leads to a smaller kinetic energy. Moreover, the TM1m model exhibits less attraction by σ mesons and weaker repulsion by ω mesons, compared to the TM1e and TM1 models. Relativistic effects are well known to increase with density, which can yield relatively smaller kinetic energy for particles with larger mass, especially at higher densities.

The curve of the SFHo model for $Y_p = 0.5$ is lower than that of TM1m. This is mainly because the incompressibility in the SFHo model ($K = 245$ MeV) is significantly smaller than that in the TM1m model ($K = 281$ MeV), despite its effective mass being even smaller. It is well known that a small value of K results in a slowly rising E/A curve for symmetric nuclear matter as the density increases. On the other hand, the results of the SLy4 model are very close to that of SFHo. Comparing these two models, the nonrelativistic Skyrme-SLy4 model has $M^*/M = 0.69$, which is smaller than the $M^*/M = 0.76$ of the SFHo model and is helpful for raising the E/A curve. However, a slightly larger K and relativistic effects in the SFHo model almost balance out the discrepancy induced by M^*/M . Ultimately, both the SFHo and SLy4 models yield remarkably similar E/A curves for symmetric nuclear matter. In the case of neutron matter ($Y_p = 0$), significant differences are observed be-

tween these models, which are caused by the differences in the symmetry energy slope L and relativistic effects. For example, the original TM1 model has a rather large value of $L = 111$ MeV, which leads to a rapidly rising E/A . In contrast, all other models considered here have similar small values of L , so the differences between them are likely attributed to different M^*/M and relativistic effects.

In Figure 2, we show the effective nucleon mass M^* as a function of the baryon number density n_B . It is seen that the TM1e model maintains the exact same behavior for M^* as the original TM1 model, whereas M^* in the TM1m model is notably larger than that in TM1.

The effective masses obtained from the SFHo and SLy4 models are also depicted for comparison, falling between those of the TM1m and TM1e models. The effective mass is known to play a key role in neutrino emission processes (Yasin et al. 2020), motivating us to explore the effects caused by the effective mass on the realistic EOS table. On the other hand, the effective mass is closely related to the spin-orbit splittings in finite nuclei—namely, a larger Dirac mass corresponds to a smaller spin-orbit splitting. The behavior of spin-orbit splittings can be improved by introducing an additional tensor interaction, which does not contribute to uniform matter at high densities (Typel & Alvear Terrero 2020).

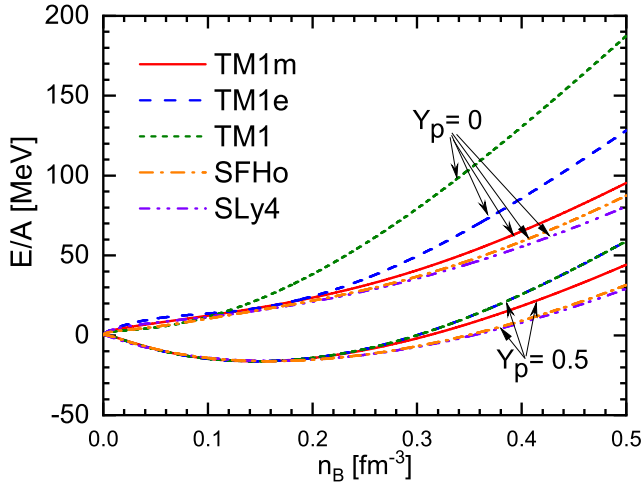


Figure 1. Energy per baryon E/A of symmetric nuclear matter and neutron matter as a function of the baryon number density n_B .

In Figure 3, we display the symmetry energy E_{sym} as a function of the baryon number density n_B . At higher densities, E_{sym} in the TM1e model is lower than that in the original TM1 model. This is because the TM1e model has a relatively smaller slope parameter ($L = 40$ MeV) than the TM1 model ($L = 111$ MeV). On the

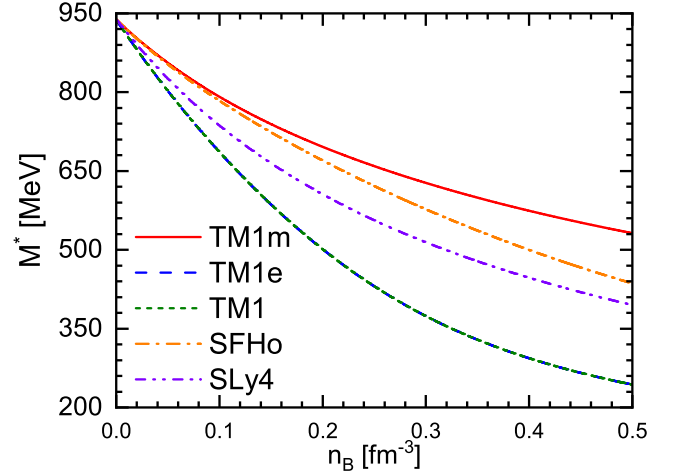


Figure 2. Effective nucleon mass M^* as a function of the baryon number density n_B .

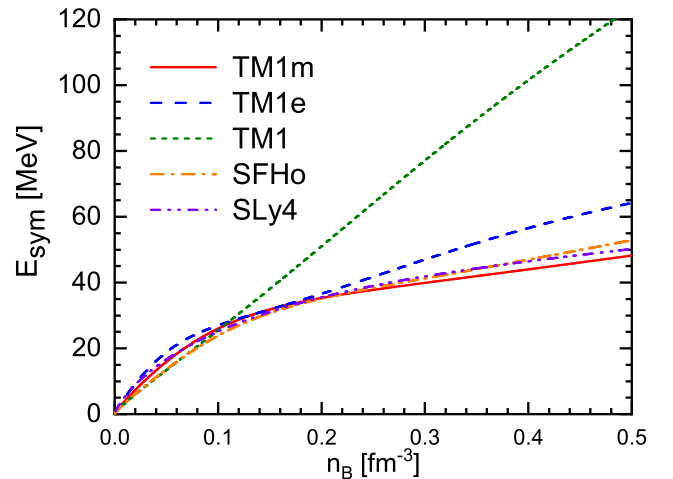


Figure 3. Symmetry energy E_{sym} as a function of the baryon number density n_B .

other hand, E_{sym} in the TM1m model is slightly lower than that in the TM1e model, which is more evident with increasing density. Although the TM1m model has the same slope parameter ($L = 40$ MeV) as the TM1e model, its larger effective mass, together with the smaller coupling constants g_σ and g_ω , can reduce the relativistic effects and lead to smaller E_{sym} at higher densities. It is noteworthy that these three models have the same values of E_{sym} at a density of 0.11 fm^{-3} . This is because the model parameters are chosen to keep E_{sym} fixed at the density of 0.11 fm^{-3} . This choice is due to the fact that the binding energies of finite nuclei are essentially determined by the symmetry energy at a density of 0.11 fm^{-3} , not by the symmetry energy at saturation density (Zhang & Chen 2013; Bao et al. 2014).

It is seen that the values of E_{sym} in the SFHo and SLy4 models are very close to those in the TM1m model. This is because these models have similar slope parameters L and effective masses M^* , as shown in Table 2.

To construct a realistic EOS table for general usage in astrophysical simulations, we should perform calculations covering a wide range of temperatures T , proton fractions Y_p , and baryon mass densities ρ_B . For uniform nuclear matter at densities above $\sim 10^{14}$ g/cm³, all required quantities can be derived within the RMF framework. To ensure completeness, we present the key thermodynamic quantities of uniform nuclear matter: the energy density ϵ , entropy density s , and pressure p . The energy density in the TM1m model is given by

$$\begin{aligned} \epsilon = & \sum_{i=p,n} \frac{1}{\pi^2} \int_0^\infty dk k^2 \sqrt{k^2 + M^{*2}} (f_{i+}^k + f_{i-}^k) \\ & + \frac{1}{2} m_\sigma^2 \sigma^2 + \frac{1}{3} g_2 \sigma^3 + \frac{1}{4} g_3 \sigma^4 + \frac{1}{2} m_\omega^2 \omega^2 \\ & + \frac{3}{4} c_3 \omega^4 + \frac{1}{2} m_\rho^2 \rho^2 + 3\Lambda_\nu (g_\omega^2 \omega^2) (g_\rho^2 \rho^2), \end{aligned} \quad (2)$$

the entropy density is written as

$$\begin{aligned} s = & - \sum_{i=p,n} \frac{1}{\pi^2} \int_0^\infty dk k^2 [f_{i+}^k \ln f_{i+}^k \\ & + (1 - f_{i+}^k) \ln (1 - f_{i+}^k) \\ & + f_{i-}^k \ln f_{i-}^k + (1 - f_{i-}^k) \ln (1 - f_{i-}^k)], \end{aligned} \quad (3)$$

and the pressure is given by

$$\begin{aligned} p = & \sum_{i=p,n} \frac{1}{3\pi^2} \int_0^\infty dk k^2 \frac{k^2}{\sqrt{k^2 + M^{*2}}} (f_{i+}^k + f_{i-}^k) \\ & - \frac{1}{2} m_\sigma^2 \sigma^2 - \frac{1}{3} g_2 \sigma^3 - \frac{1}{4} g_3 \sigma^4 + \frac{1}{2} m_\omega^2 \omega^2 \\ & + \frac{1}{4} c_3 \omega^4 + \frac{1}{2} m_\rho^2 \rho^2 + \Lambda_\nu (g_\omega^2 \omega^2) (g_\rho^2 \rho^2). \end{aligned} \quad (4)$$

Here, $M^* = M + g_\sigma \sigma$ denotes the effective nucleon mass. f_{i+}^k and f_{i-}^k ($i = p, n$) are the occupation probabilities of nucleons and antinucleons at momentum k , respectively, which are given by the Fermi-Dirac distribution:

$$f_{i\pm}^k = \left\{ 1 + \exp \left[\left(\sqrt{k^2 + M^{*2}} \mp \nu_i \right) / T \right] \right\}^{-1}. \quad (5)$$

The kinetic part of the chemical potential ν_i is related to the chemical potential μ_i as

$$\mu_i = \nu_i + g_\omega \omega + \frac{g_\rho}{2} T_{3i} \rho. \quad (6)$$

The number density of protons ($i = p$) or neutrons ($i = n$) can be obtained by

$$n_i = \frac{1}{\pi^2} \int_0^\infty dk k^2 (f_{i+}^k - f_{i-}^k). \quad (7)$$

The free-energy density is given by $f = \epsilon - Ts$. Within the RMF model for uniform matter, these thermodynamic quantities satisfy the self-consistent relation

$$f = \sum_{i=p,n} \mu_i n_i - p. \quad (8)$$

3. RESULTS AND DISCUSSION

In this section, we present numerical results using the TM1m model with a larger effective mass, while also conducting an in-depth comparison with the TM1e and original TM1 models. First, we discuss the properties of neutron stars at zero temperature and check the compatibility with current observations. Second, we show the results of the new EOS table (EOS5), especially at densities higher than $\sim 10^{14}$ g/cm³, in order to explore the impact of the effective nucleon mass on the EOS table.

3.1. Neutron stars at zero temperature

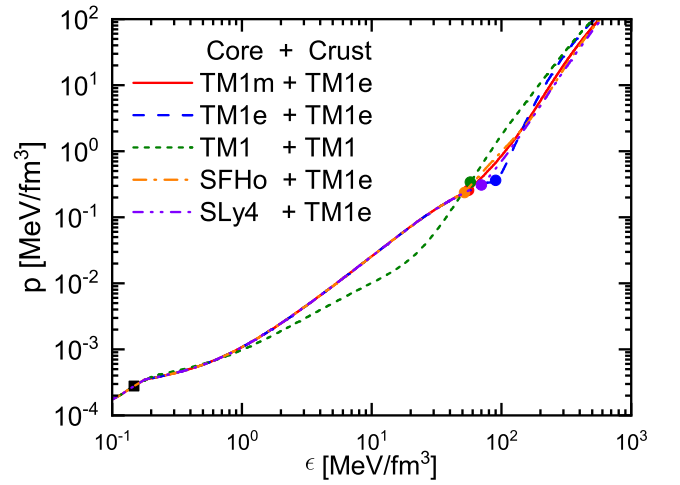


Figure 4. Pressure p as a function of the energy density ϵ . The core EOSs are obtained within the models considered in this work. The inner crust is described in the Thomas-Fermi approximation using the TM1e and TM1 models. The crust-core transition is indicated by the filled circles. The BPS EOS is adopted for the outer crust and the matching point is marked by the filled square.

The properties of static neutron stars can be obtained by solving the well-known Tolman-Oppenheimer-Volkoff equation with the EOS over a wide range of densities. The neutron star matter is assumed to be in beta equilibrium with the charge neutrality at zero temperature. Generally, the EOS used for the calculations of the neutron star structure can be divided into at least three segments: (a) the EOS of the outer crust below the neutron drip density; (b) the EOS of the inner crust from the

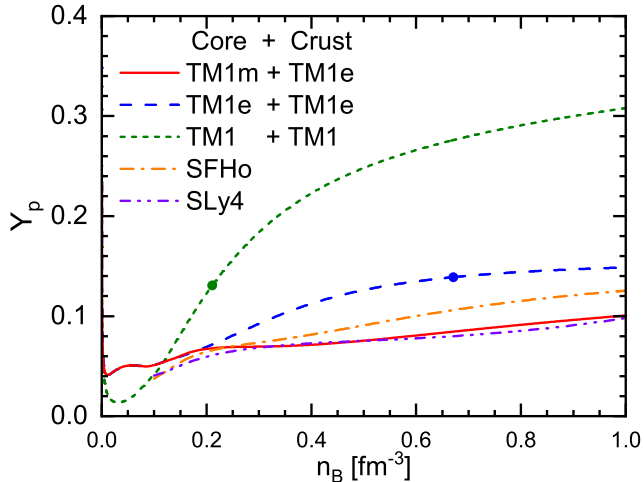


Figure 5. Proton fraction Y_p as a function of the baryon density n_B . The filled circles indicate the threshold for the DUrca process.

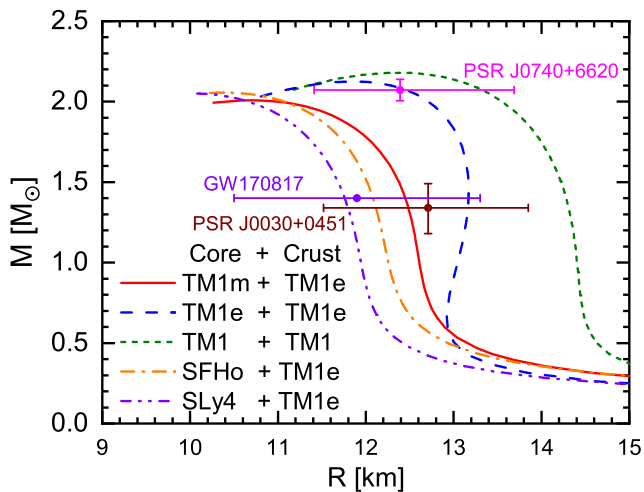


Figure 6. Mass-radius relations of neutron stars obtained using the EOSs shown in Figure 4. The horizontal violet line represents the constraint on $R_{1.4}$ inferred from GW170817 (Abbott et al. 2018). The horizontal brown and magenta lines correspond to simultaneous measurements of the mass and radius from NICER for PSR J0030+0451 (Riley et al. 2019) and PSR J0740+6620 (Riley et al. 2021), respectively.

neutron drip to crust-core transition; and (c) the EOS of the liquid core above the crust-core transition. In the present work, we use the Baym-Pethick-Sutherland (BPS) EOS (Baym et al. 1971) for the outer crust, while the inner crust EOS is based on the self-consistent Thomas-Fermi approximation using both TM1e ($L = 40$ MeV) and TM1 ($L = 111$ MeV) parameterizations (Ji et al. 2019).

The EOS of the liquid core above the crust-core transition is calculated in the RMF approach using the TM1m, TM1e, and TM1 parameterizations, while the results of the SFHo and SLy4 models are also depicted for comparison. The core EOS is connected to the inner-crust EOS at their crossing point. In Figure 4, we show the pressure p as a function of the energy density ϵ . It is shown that the TM1m model predicts relatively small pressures at high densities, while the TM1 EOS is stiffer than the other cases. We note that the EOSs with TM1e (blue dashed line) and TM1 (green dotted line) are unified EOSs, because their inner-crust and core segments are obtained within the same nuclear model. It is seen that the core EOSs obtained from the SFHo and SLy4 models are very close to the TM1m model.

In Figure 5, the proton fraction Y_p is plotted as a function of the baryon density n_B , and the corresponding threshold density for the DUrca process is indicated by the filled circles. It is well known that the DUrca process can occur for $Y_p \geq 1/9$ in a simple npe matter, while the critical Y_p for the DUrca process is in the range of (11.1–14.8)% when the muons are included under the equilibrium condition $\mu_e = \mu_\mu$ (Lattimer et al. 1991). The original TM1 model ($L = 111$ MeV) predicts higher Y_p and a smaller DUrca threshold density ($\sim 0.21 \text{ fm}^{-3}$).

The results of TM1e are lower than those of TM1, while its DUrca threshold density is about 0.67 fm^{-3} . The curves of TM1m, SFHo, and SLy4 are close to each other and lie lower than those of TM1 and TM1e. The behaviors of Y_p are mainly determined by the symmetry energies, as illustrated in Figure 3. Due to the small symmetry energies in TM1m, SFHo, and SLy4, these models yield relatively small Y_p in neutron star matter. As a result, the critical Y_p for the DUrca process could not be reached in these models. It is well known that the DUrca process is the fastest neutrino emission mechanism ever known. Once it is turned on, the neutron star cooling is predominantly controlled by the DUrca process, which leads to a rapid drop in the cooling curve, known as fast cooling. According to observational data in the temperature-age diagram, the DUrca process is unlikely to occur in neutron stars with masses below $1.5 M_\odot$, since it would lead to an unacceptably fast cooling, in disagreement with the observations (Fantina et al. 2013). On the other hand, for the TM1m, SFHo, and SLy4 models, where the DUrca process is forbidden, the thermal evolution of neutron stars is regulated by several slow cooling processes, such as the modified Urca and bremsstrahlung, which result in higher temperatures than the observations of middle-age stars (Lim et al. 2017). Additional cooling processes, related to the

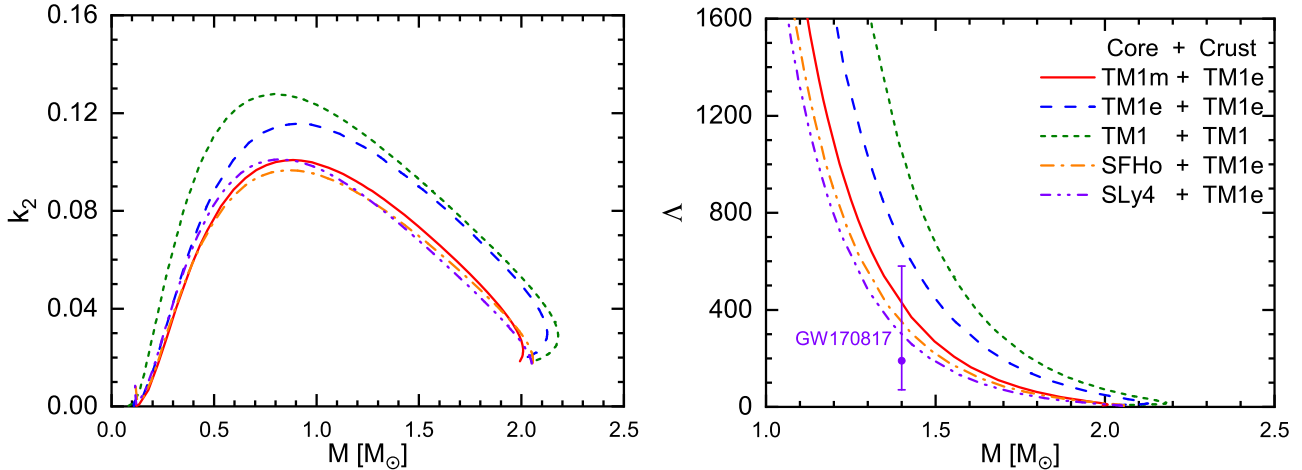


Figure 7. Love number k_2 and tidal deformability Λ as a function of the neutron star mass M . The vertical violet line represents the constraint on $\Lambda_{1.4}$ inferred from GW170817 (Abbott et al. 2018).

presence of hyperons and superfluidity, have also been discussed in the literature (Fortin et al. 2021), but this is beyond the scope of the present paper.

In Figure 6, we display the predicted mass-radius relations of neutron stars using the EOSs shown in Figure 4, along with several constraints from astrophysical observations. It is found that the maximum masses of neutron stars predicted by the TM1m, TM1e, and TM1 models are about 2.01 , 2.12 , and $2.18 M_\odot$, respectively, which fulfill the observational constraints on the maximum mass $M_{\max} > 2 M_\odot$. The mass-radius relations exhibit significant variations among these models, which are caused by different behaviors of the symmetry energy and its slope, as shown in Figure 3. For the radius of a canonical $1.4 M_\odot$ neutron star, denoted as $R_{1.4}$, a large value of ~ 14.2 km is obtained using the TM1 model, while it reduces to 13.1 km in the TM1e model and 12.4 km in the TM1m model, respectively.

The results obtained from the SFHo and SLy4 models are also depicted for comparison. The maximum masses of the neutron stars obtained from the SFHo and SLy4 models are about $2.06 M_\odot$, while the values of $R_{1.4}$ are 12.1 km and 11.7 km, respectively. The analysis of GW170817 data provides a constraint on $R_{1.4}$, with an estimated value of $R_{1.4} = 11.9 \pm 1.4$ km (Abbott et al. 2018). The resulting $R_{1.4}$ within these models, except TM1, can be compatible with the constraint inferred from GW170817, which is closely related to the symmetry energy slope L . Generally, a smaller value of L leads to a smaller $R_{1.4}$.

The observation of gravitational waves from GW170817 has provided valuable insights and constraints on the tidal deformability of neutron stars. Theoretically, the tidal deformability Λ can be calculated using the EOS through both the tidal Love number

k_2 and the compactness parameter $C = M/R$, following the relation $\Lambda = \frac{2}{3}k_2C^{-5}$ (Ji et al. 2019). In Figure 7, we show the tidal Love number k_2 (left panel) and the dimensionless tidal deformability Λ (right panel) as a function of the neutron star mass M . It is observed that k_2 rises as the neutron star mass increases, achieving its maximum at a mass of around 0.7 to $0.9 M_\odot$. Subsequently, in the more massive range, k_2 exhibits a rapid reduction. It is noticeable that the TM1m model predicts a smaller k_2 value compared to the TM1e and TM1 models, leading to a lower tidal deformability Λ within the TM1m model, as illustrated in the right panel of Figure 7. Generally, the value of Λ is very large for a small neutron star mass due to its small compactness parameter C . As the star mass increases, the tidal deformability Λ decreases rapidly. The analysis of GW170817 has provided a constraint on the tidal deformability of a $1.4 M_\odot$ neutron star, i.e., $70 \leq \Lambda_{1.4} \leq 580$ (Abbott et al. 2018). The resulting $\Lambda_{1.4}$ in the TM1m, SFHo, and SLy4 models are compatible with the constraint inferred from the analysis of GW170817.

3.2. Supernova matter at finite temperature

To explore the influence of the effective nucleon mass on astrophysical simulations such as core-collapse supernovae and binary neutron star mergers, we construct a new EOS table (EOS5) using the TM1m model. All quantities listed in the EOS table, as detailed in Appendix A of Shen et al. (2011b), are calculated using the TM1m model for uniform matter at densities higher than $\sim 10^{14}$ g/cm³, which can then be combined with the nonuniform part of the Shen EOS4 at low densities to generate the final EOS table, as is often done in the literature Ishizuka et al. (2008); Sumiyoshi et al. (2019).

As illustrated in Figures 1-3, the discrepancies between the TM1m and TM1e models become increasingly evident as the density increases. Consequently, our analysis focuses on a detailed comparison of uniform matter at high densities. There will be a separate work on the low-density part of the EOS table elsewhere.

The EOS table covers a wide range of temperatures T , proton fractions Y_p , and baryon mass densities ρ_B for use in numerical simulations of core-collapse supernovae, proto-neutron star cooling, and binary neutron star mergers. For convenience in practical use, we provide the EOS table in the same tabular form as given in Table 1 of Shen et al. (2011b), which has been extensively adopted by the EOSs posted on the public database CompOSE. In general, when the temperature is higher than a critical value of ~ 14 MeV and the density is beyond $\sim 10^{14.1}$ g/cm³, heavy nuclei dissolve and the favorable state is uniform nuclear matter.

In Figure 8, we display the effective nucleon mass M^* as a function of the baryon mass density ρ_B at $T = 1$ and 10 MeV. Although the calculations are performed at $Y_p = 0.5$, the results of M^* are found to be rather insensitive to Y_p . This is because M^* is determined by the scalar meson σ , according to the relation $M^* = M + g_\sigma \sigma$. Notably, the effective masses in the TM1e and TM1 models are identical, due to having the same isoscalar properties. The results obtained in the TM1m model (red solid lines) are significantly larger than those of TM1e (blue dashed lines) and TM1 (green dotted lines). It is shown that M^* decreases as the density increases. At the saturation density n_0 ($\rho_B \simeq 10^{14.4}$ g/cm³), the effective masses obtained in the TM1m and TM1e models are, respectively, $M^* = 744$ MeV and $M^* = 595$ MeV. When the density rises to $\rho_B = 10^{15}$ g/cm³ (about $4n_0$), the effective masses decrease to $M^* = 496$ MeV in the TM1m model and $M^* = 210$ MeV in the TM1e model, respectively.

The effective masses obtained from the SFHo and SLy4 models show a similar density dependence, while the values fall between those of the TM1m and TM1e models. Comparing the case at $T = 10$ MeV in the upper panel with that at $T = 1$ MeV in the lower panel, the behaviors of the effective masses are similar. This suggests that the effective mass has a rather weak dependence on temperature.

It is essential to investigate how the effective mass influences the thermodynamic quantities within the EOS table.

In Figure 9, we show the entropy per baryon S as a function of ρ_B for $Y_p = 0.1$ and 0.5 at $T = 1$ and 10 MeV. It is observed that the values of S significantly decrease with increasing density. One can see that, around

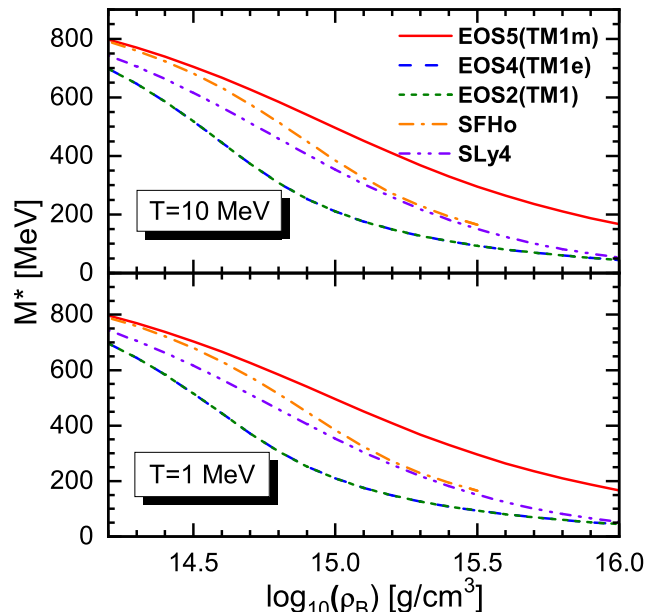


Figure 8. Effective nucleon mass M^* as a function of the baryon mass density ρ_B at $T = 1$ and 10 MeV. The results are obtained for symmetric nuclear matter ($Y_p = 0.5$).

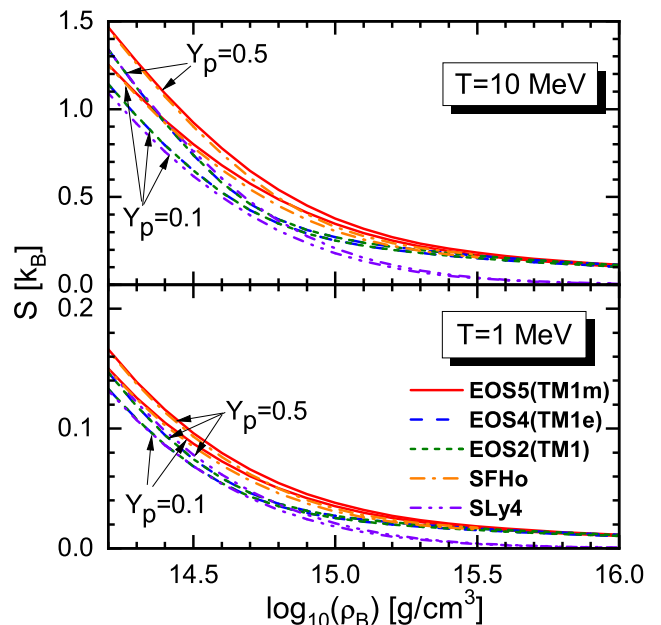


Figure 9. Entropy per baryon S as a function of the baryon mass density ρ_B with $Y_p = 0.1$ and 0.5 at $T = 1$ and 10 MeV.

the saturation density, there are noticeable differences among the models considered in this work. However, the differences among all RMF models (TM1, TM1e, TM1m, and SFHo) nearly disappear at higher densities. Meanwhile, the deviation between the nonrelativistic SLy4 model and the RMF models remains finite, especially in the high-density region. This deviation is

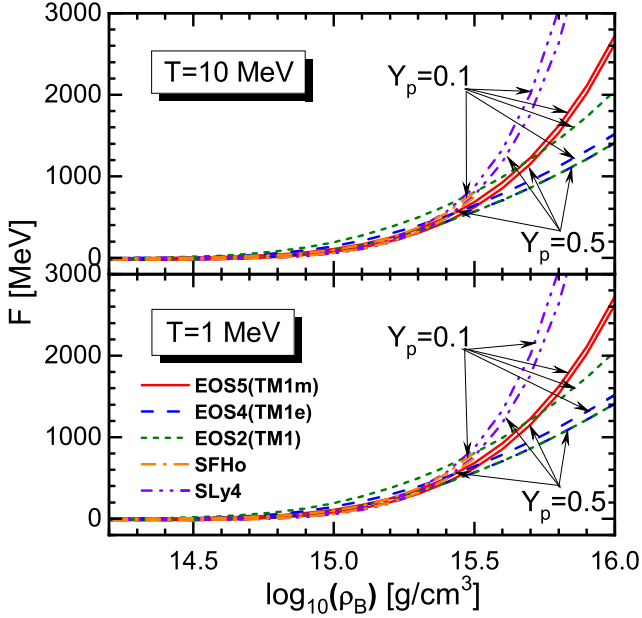


Figure 10. The same as Figure 9, but for the free energy per baryon F .

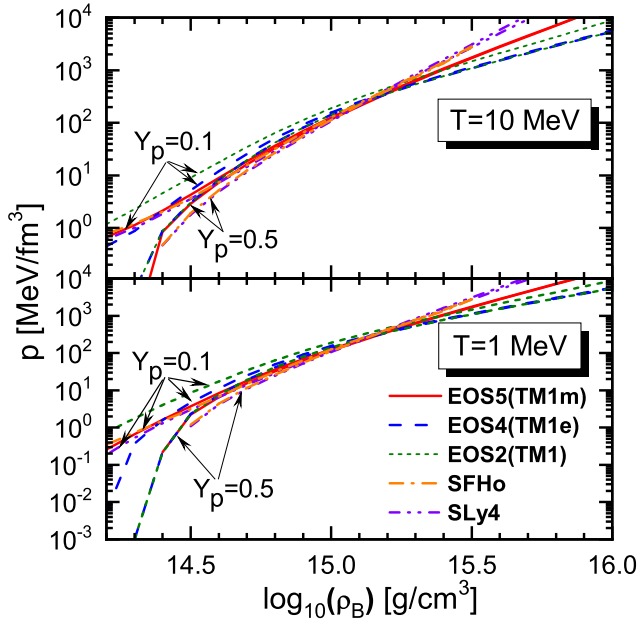


Figure 11. The same as Figure 9, but for the pressure p .

caused by a nonrelativistic calculation for S used in the SLy4 model (Schneider et al. 2017). When the relativistic formula $\sqrt{k^2 + M^{*2}}$ in Equation (5) is simply replaced by a nonrelativistic approximation $M^* + k^2/2M^*$, the entropy per baryon S obtained in the TM1m model gradually approaches the results of the nonrelativistic SLy4 model with increasing density, which verifies that the deviation in S at higher densities between the TM1m

and SLy4 models is mainly due to relativistic effects. From Equations (3) and (5), it is seen that the entropy S is closely related to the effective mass M^* . The discrepancies between these models can be understood by analyzing the behaviors of M^* , as shown in Figure 8. On the other hand, the difference of the symmetry energy between the TM1 and TM1e models has a minor influence on the entropy. It is worth noting that the entropy values at $T = 10$ MeV (upper panel) are roughly ten times greater than those of $T = 1$ MeV (lower panel). Generally, the differences between $Y_p = 0.1$ and 0.5 decrease as the density increases.

In Figure 10, we plot the free energy per baryon F as a function of the baryon mass density ρ_B for $Y_p = 0.1$ and 0.5 at $T = 1$ and 10 MeV. We first compare the results in EOS5 (TM1m) with those in EOS4 (TM1e) and EOS2 (TM1). At densities below $\rho_B \simeq 10^{15.4}$ g/cm³ (about $10n_0$), the free energies in the TM1m model are lower than those in the TM1e model, which can be more easily observed in Figure 1. This is because the larger effective mass in the TM1m model leads to a relatively smaller kinetic energy. However, at extremely high densities, the free energies in the TM1m model exceed those in the TM1e model, owing to the growing contributions from nonlinear meson terms.

For comparison, the results obtained from the SFHo and SLy4 models are also plotted in this figure. At densities below $\rho_B \simeq 10^{15.5}$ g/cm³, the behaviors of F in the SFHo and SLy4 models are similar to those in the TM1m model, due to their similar saturation properties. When $\rho_B > 10^{15.5}$ g/cm³, the SFHo model fails to obtain physical solutions for the field equations. Consequently, the maximum density in the SFHo EOS table on CompOSE is set at $10^{15.5}$ g/cm³ (1.9 fm⁻³). On the other hand, the nonrelativistic SLy4 model yields significantly larger F than the TM1m model at densities higher than $\sim 10^{15.5}$ g/cm³. This discrepancy is primarily due to the distinct density-dependent behaviors, which gradually become more apparent as the density increases. As for the dependence on Y_p , it is noteworthy that the differences between the results of $Y_p = 0.5$ and $Y_p = 0.1$ are clearly model-dependent. In contrast to other models, the original TM1 model presents considerably larger differences between $Y_p = 0.5$ and $Y_p = 0.1$. This is because the TM1 model exhibits significantly larger symmetry energies at higher densities, as shown in Figure 3. Comparing the free-energy trends between $T = 1$ MeV and $T = 10$ MeV, it is observed that they are very similar.

In Figure 11, we display the pressure p as a function of ρ_B for $Y_p = 0.1$ and 0.5 at $T = 1$ and 10 MeV. According to tradition, when constructing an EOS table, the con-

tributions from leptons and photons are usually calculated separately, so they are not included in the present work. As shown in Figure 11, it is evident that at low densities, the pressure values are very small, even reaching negative levels when $Y_p = 0.5$. It is known that the pressure of leptons and photons is significantly higher than that of baryons around the saturation density, and the total pressure becomes positive when the contributions from leptons and photons are taken into account. With increasing density, the pressure rises rapidly.

The discrepancies between the different models are density-dependent. At densities below $\rho_B \simeq 10^{15.2} \text{ g/cm}^3$, the pressures in the TM1 model with $Y_p = 0.1$ are visibly higher than those in other models, which is caused by the larger symmetry energy slope L . It has been pointed out in [Oyamatsu & Iida \(2007\)](#) that a larger value of L implies a higher pressure of pure neutron matter. At extremely high densities, the pressure values in the different models exhibit distinct density-dependent behaviors. This is due to the increasing influence of nonlinear meson terms.

4. SUMMARY

In this work, we have investigated the influence of the effective nucleon mass on the EOS for astrophysical simulations such as core-collapse supernovae, proto-neutron star cooling, and binary neutron star mergers. We have employed the RMF model, in which the effective nucleon mass is more consistently integrated than it is in nonrelativistic approaches such as the Skyrme model. A new RMF parameter set, TM1m, is introduced in the present work, which is a modification of the TM1e parameterization with a larger effective mass. The TM1m model preserves the same saturation properties as the TM1e model, but their effective masses are significantly different: $M^*/M \sim 0.8$ for the TM1m model and $M^*/M \sim 0.63$ for the TM1e model. It is well known that there exists a positive correlation between the symmetry energy slope L and the neutron star radius. In contrast to the original TM1 model characterized by $L = 111 \text{ MeV}$, both the TM1m and TM1e models provide a small value of $L = 40 \text{ MeV}$, which is more favored by recent astrophysical observations.

We calculate the properties of cold neutron stars using the TM1m model and compare with the results obtained by the TM1e and TM1 models.

For comparison, we also include the results from an RMF model with the SFHo parameterization and a non-relativistic Skyrme model with the SLy4 parameterization. The maximum masses of neutron stars obtained in these models could fulfill the observational constraint $M_{\text{max}} > 2 M_\odot$. It is found that the mass-radius rela-

tions exhibit significant variations among these models, which might be caused by different behaviors of the symmetry energy and its slope. Regarding the radius of a canonical $1.4 M_\odot$ neutron star ($R_{1.4}$), a large value of $\sim 14.2 \text{ km}$ is obtained using the TM1 model, which is reduced to 13.1 km in the TM1e model and 12.4 km in the TM1m models, respectively. The resulting radius $R_{1.4}$ and the tidal deformability $\Lambda_{1.4}$ within the TM1m model could be compatible with the constraint inferred from the gravitational-wave event GW170817.

To explore the impact of the effective nucleon mass in astrophysical simulations such as core-collapse supernovae and binary neutron star mergers, we have constructed a new EOS table (EOS5) using the TM1m model. All quantities included in the EOS table are calculated using the TM1m model for uniform matter at densities higher than $\sim 10^{14} \text{ g/cm}^3$, which could be combined with the nonuniform part of the Shen EOS4 at low densities to generate the final EOS table. It is shown that the effective nucleon mass M^* significantly decreases as the density increases. At supra-saturation densities, the TM1m model predicts lower free energies and pressures than the TM1e model, which may be due to the fact that the larger effective masses in the TM1m model result in relatively smaller kinetic energies. However, at extremely high densities, the free energies in the TM1m model exceed those in the TM1e model, owing to the growing contributions from nonlinear meson terms.

Compared to the TM1m model, the SFHo model has similar saturation properties, with $M^*/M \sim 0.76$, which yield comparable results in the EOS table. At higher densities, the nonrelativistic SLy4 model predicts smaller entropy and larger free energy than the RMF models. The new EOS table (EOS5), constructed using the TM1m model, offers a valuable resource for exploring the influence of the effective nucleon mass on the dynamics of supernovae within the same parameterization family. The advantage of conducting a comparison between the TM1m and TM1e EOS tables lies in the fact that only the effective masses differ while the other saturation properties remain identical. Numerical simulations of core-collapse supernovae, as well as analyses of the influence of the effective nucleon mass, are currently underway.

5. ACKNOWLEDGMENTS

This work was supported in part by the National Natural Science Foundation of China (grant Nos. 12175109 and 12475149) and the Natural Science Foundation of Guangdong Province (grant No: 2024A1515010911). K.S. is supported by Grant-in-Aid for Scientific Research (19K03837, 20H01905, and 24K00632) from the Min-

istry of Education, Culture, Sports, Science and Technology (MEXT), Japan. K.S. acknowledges the Computing Research Center, KEK, JLDG on SINET of NII, the Research Center for Nuclear Physics, Osaka University, the Yukawa Institute of Theoretical Physics, Kyoto University, Nagoya University, and the Information Technology Center, University of Tokyo, for providing high-performance computing resources. K.S. is partly supported by MEXT via the “Program for Promoting

Researches on the Supercomputer Fugaku” (Structure and Evolution of the Universe Unraveled by the Fusion of Simulation and AI, JPMXP1020230406, Project IDs: hp230204, hp230270, hp240219, and hp240264), the HPCI System Research Project (Project IDs: hp230056 and hp240041), and the Particle, Nuclear and Astro Physics Simulation Program (No. 2023-003) of the Institute of Particle and Nuclear Studies, High Energy Accelerator Research Organization (KEK).

REFERENCES

- Abbott, B. P., Abbott, R., Abbott, T., et al. 2017, *Physical Review Letters*, 119, 161101
- . 2018, *Physical Review Letters*, 121, 161101, doi: [10.1103/PhysRevLett.121.161101](https://doi.org/10.1103/PhysRevLett.121.161101)
- Andersen, O. E., Zha, S., da Silva Schneider, A., et al. 2021, *The Astrophysical Journal*, 923, 201, doi: [10.3847/1538-4357/ac294c](https://doi.org/10.3847/1538-4357/ac294c)
- Antoniadis, J., Freire, P. C. C., Wex, N., et al. 2013, *Science*, 340, 1233232, doi: [10.1126/science.1233232](https://doi.org/10.1126/science.1233232)
- Arzoumanian, Z., Brazier, A., Burke-Spolaor, S., et al. 2018, *The Astrophysical Journal Supplement Series*, 235, 37, doi: [10.3847/1538-4365/aab5b0](https://doi.org/10.3847/1538-4365/aab5b0)
- Bao, S., Hu, J., Zhang, Z., & Shen, H. 2014, *Physical Review C*, 90, 045802, doi: [10.1103/PhysRevC.90.045802](https://doi.org/10.1103/PhysRevC.90.045802)
- Baym, G., Bethe, H. A., & Pethick, C. J. 1971, *Nuclear Physics A*, 175, 225, doi: [https://doi.org/10.1016/0375-9474\(71\)90281-8](https://doi.org/10.1016/0375-9474(71)90281-8)
- Chabanat, E., Bonche, P., Haensel, P., Meyer, J., & Schaeffer, R. 1998, *Nuclear Physics A*, 635, 231, doi: [https://doi.org/10.1016/S0375-9474\(98\)00180-8](https://doi.org/10.1016/S0375-9474(98)00180-8)
- Chen, W.-C., & Piekarewicz, J. 2014, *Physical Review C*, 90, 044305, doi: [10.1103/PhysRevC.90.044305](https://doi.org/10.1103/PhysRevC.90.044305)
- . 2015, *Physics Letters B*, 748, 284, doi: <https://doi.org/10.1016/j.physletb.2015.07.020>
- Choi, S., Miyatsu, T., Cheoun, M.-K., & Saito, K. 2021, *The Astrophysical Journal*, 909, 156, doi: [10.3847/1538-4357/abe3fe](https://doi.org/10.3847/1538-4357/abe3fe)
- Dutra, M., Lourenço, O., Avancini, S., et al. 2014, *Physical Review C*, 90, 055203
- Fantina, A., Chamel, N., Pearson, J., & Goriely, S. 2013, *Astronomy & astrophysics*, 559, A128, doi: [10.1051/0004-6361/201321884](https://doi.org/10.1051/0004-6361/201321884)
- Fattoyev, F. J., Horowitz, C. J., Piekarewicz, J., & Shen, G. 2010, *Physical Review C*, 82, 055803, doi: [10.1103/PhysRevC.82.055803](https://doi.org/10.1103/PhysRevC.82.055803)
- Fattoyev, F. J., Piekarewicz, J., & Horowitz, C. J. 2018, *Physical Review Letters*, 120, 172702, doi: [10.1103/PhysRevLett.120.172702](https://doi.org/10.1103/PhysRevLett.120.172702)
- Fonseca, E., Cromartie, H. T., Pennucci, T. T., et al. 2021, *The Astrophysical Journal Letters*, 915, L12, doi: [10.3847/2041-8213/ac03b8](https://doi.org/10.3847/2041-8213/ac03b8)
- Fortin, M., Raduta, A. R., Avancini, S., & Providência, C. m. c. 2021, *Physical Review D*, 103, 083004, doi: [10.1103/PhysRevD.103.083004](https://doi.org/10.1103/PhysRevD.103.083004)
- Furusawa, S., Sumiyoshi, K., Yamada, S., & Suzuki, H. 2017a, *Nuclear Physics A*, 957, 188, doi: <https://doi.org/10.1016/j.nuclphysa.2016.09.002>
- Furusawa, S., Togashi, H., Nagakura, H., et al. 2017b, *Journal of Physics G: Nuclear and Particle Physics*, 44, 094001
- Furusawa, S., Togashi, H., Sumiyoshi, K., et al. 2020, *Progress of Theoretical and Experimental Physics*, 2020, 013D05, doi: [10.1093/ptep/ptz135](https://doi.org/10.1093/ptep/ptz135)
- Hempel, M., & Schaffner-Bielich, J. 2010, *Nuclear Physics A*, 837, 210, doi: <https://doi.org/10.1016/j.nuclphysa.2010.02.010>
- Huang, K., Hu, J., Zhang, Y., & Shen, H. 2022a, *The Astrophysical Journal*, 935, 88, doi: [10.3847/1538-4357/ac7f3c](https://doi.org/10.3847/1538-4357/ac7f3c)
- . 2022b, *Nuclear Physics Review*, 39, 135, doi: [10.11804/NuclPhysRev.39.2022013](https://doi.org/10.11804/NuclPhysRev.39.2022013)
- Ishizuka, C., Ohnishi, A., Tsubakihara, K., Sumiyoshi, K., & Yamada, S. 2008, *Journal of Physics G: Nuclear and Particle Physics*, 35, 085201, doi: [10.1088/0954-3899/35/8/085201](https://doi.org/10.1088/0954-3899/35/8/085201)
- Ji, F., Hu, J., Bao, S., & Shen, H. 2019, *Physical Review C*, 100, 045801
- Lalazisis, G., König, J., & Ring, P. 1997, *Physical Review C*, 55, 540
- Lattimer, J. M., Pethick, C. J., Prakash, M., & Haensel, P. 1991, *Physical Review Letters*, 66, 2701, doi: [10.1103/PhysRevLett.66.2701](https://doi.org/10.1103/PhysRevLett.66.2701)
- Lattimer, J. M., & Swesty, F. D. 1991, *Nuclear Physics A*, 535, 331, doi: [https://doi.org/10.1016/0375-9474\(91\)90452-C](https://doi.org/10.1016/0375-9474(91)90452-C)
- Lim, Y., Hyun, C. H., & Lee, C.-H. 2017, *International Journal of Modern Physics E*, 26, 1750015

- Maruyama, T., Chiba, S., Schulze, H.-J., & Tatsumi, T. 2007, *Physical Review D*, 76, 123015, doi: [10.1103/PhysRevD.76.123015](https://doi.org/10.1103/PhysRevD.76.123015)
- Miller, M. C., Lamb, F. K., Dittmann, A. J., et al. 2019, *The Astrophysical Journal Letters*, 887, L24, doi: [10.3847/2041-8213/ab50c5](https://doi.org/10.3847/2041-8213/ab50c5)
- . 2021, *The Astrophysical Journal Letters*, 918, L28, doi: [10.3847/2041-8213/ac089b](https://doi.org/10.3847/2041-8213/ac089b)
- Miyatsu, T., Cheoun, M.-K., Kim, K., & Saito, K. 2024, Novel features of asymmetric nuclear matter from large neutron skin thickness and small neutron-star radii. <https://arxiv.org/abs/2411.13210>
- Most, E. R., Weih, L. R., Rezzolla, L., & Schaffner-Bielich, J. 2018, *Physical Review Letters*, 120, 261103, doi: [10.1103/PhysRevLett.120.261103](https://doi.org/10.1103/PhysRevLett.120.261103)
- Nagakura, H., Furusawa, S., Togashi, H., et al. 2019, *The Astrophysical Journal Supplement Series*, 240, 38, doi: [10.3847/1538-4365/aafac9](https://doi.org/10.3847/1538-4365/aafac9)
- Nakazato, K., & Suzuki, H. 2019, *The Astrophysical Journal*, 878, 25, doi: [10.3847/1538-4357/ab1d4b](https://doi.org/10.3847/1538-4357/ab1d4b)
- Oertel, M., Hempel, M., Klähn, T., & Typel, S. 2017, *Reviews of Modern Physics*, 89, 015007, doi: [10.1103/RevModPhys.89.015007](https://doi.org/10.1103/RevModPhys.89.015007)
- Oyamatsu, K., & Iida, K. 2007, *Physical Review C*, 75, 015801, doi: [10.1103/PhysRevC.75.015801](https://doi.org/10.1103/PhysRevC.75.015801)
- Raduta, A., & Gulminelli, F. 2019, *Nuclear Physics A*, 983, 252, doi: <https://doi.org/10.1016/j.nuclphysa.2018.11.003>
- Riley, T. E., Watts, A. L., Bogdanov, S., et al. 2019, *The Astrophysical Journal Letters*, 887, L21
- Riley, T. E., Watts, A. L., Ray, P. S., et al. 2021, *The Astrophysical Journal Letters*, 918, L27
- Schneider, A. S., Roberts, L. F., & Ott, C. D. 2017, *Physical Review C*, 96, 065802, doi: [10.1103/PhysRevC.96.065802](https://doi.org/10.1103/PhysRevC.96.065802)
- Schneider, A. S., Roberts, L. F., Ott, C. D., & O'Connor, E. 2019, *Physical Review C*, 100, 055802, doi: [10.1103/PhysRevC.100.055802](https://doi.org/10.1103/PhysRevC.100.055802)
- Serot, B. D., & Walecka, J. D. 1986, *Advances in Nuclear Physics*, edited by JW Negele and E. Vogt, Plenum, New York
- Shen, G., Horowitz, C. J., & O'Connor, E. 2011a, *Physical Review C*, 83, 065808, doi: [10.1103/PhysRevC.83.065808](https://doi.org/10.1103/PhysRevC.83.065808)
- Shen, H., Ji, F., Hu, J., & Sumiyoshi, K. 2020, *The Astrophysical Journal*, 891, 148, doi: [10.3847/1538-4357/ab72fd](https://doi.org/10.3847/1538-4357/ab72fd)
- Shen, H., Toki, H., Oyamatsu, K., & Sumiyoshi, K. 1998a, *Progress of Theoretical Physics*, 100, 1013
- . 1998b, *Nuclear Physics A*, 637, 435
- . 2011b, *The Astrophysical Journal Supplement Series*, 197, 20, doi: [10.1088/0067-0049/197/2/20](https://doi.org/10.1088/0067-0049/197/2/20)
- Steiner, A. W., Hempel, M., & Fischer, T. 2013, *The Astrophysical Journal*, 774, 17, doi: [10.1088/0004-637X/774/1/17](https://doi.org/10.1088/0004-637X/774/1/17)
- Sumiyoshi, K., Kojo, T., & Furusawa, S. 2023, *Equation of State in Neutron Stars and Supernovae* (Springer Nature Singapore), 1–51, doi: [10.1007/978-981-15-8818-1_104-1](https://doi.org/10.1007/978-981-15-8818-1_104-1)
- Sumiyoshi, K., Nakazato, K., Suzuki, H., Hu, J., & Shen, H. 2019, *The Astrophysical Journal*, 887, 110, doi: [10.3847/1538-4357/ab5443](https://doi.org/10.3847/1538-4357/ab5443)
- Togashi, H., Nakazato, K., Takehara, Y., et al. 2017, *Nuclear Physics A*, 961, 78. <https://dx.doi.org/10.1016/j.nuclphysa.2017.02.010>
- Typel, S., & Alvear Terrero, D. 2020, *The European Physical Journal A*, 56, 160, doi: [10.1140/epja/s10050-020-00172-2](https://doi.org/10.1140/epja/s10050-020-00172-2)
- Typel, S., Oertel, M., & Klähn, T. 2015, *Physics of Particles and Nuclei*, 46, 633
- Typel, S., Oertel, M., Klähn, T., et al. 2022, *The European Physical Journal A*, 58, 221. <https://compose.obspm.fr/>
- Weber, F., Farrell, D., Spinella, W. M., et al. 2019, *Universe*, 5, 169. <https://dx.doi.org/10.3390/universe5070169>
- Yasin, H., Schäfer, S., Arcones, A., & Schwenk, A. 2020, *Physical Review Letters*, 124, 092701, doi: [10.1103/PhysRevLett.124.092701](https://doi.org/10.1103/PhysRevLett.124.092701)
- Yasutake, N., Lastowiecki, R., BeniĆ, S., et al. 2014, *Physical Review C*, 89, 065803, doi: [10.1103/PhysRevC.89.065803](https://doi.org/10.1103/PhysRevC.89.065803)
- Zhang, Z., & Chen, L.-W. 2013, *Physics Letters B*, 726, 234, doi: <https://doi.org/10.1016/j.physletb.2013.08.002>